


# Near-Infrared Light-Triggered NO Nanogenerator for Gas-Enhanced Photodynamic Therapy and Low-Temperature Photothermal Therapy to Eliminate Biofilms

Junjuan Li<sup>1,\*</sup>, Yue Tian<sup>2,\*</sup>, Qi Qin<sup>2,\*</sup>, Zhaolei Ding<sup>1</sup>, Xue Zhao<sup>3</sup>, Wei Tan<sup>1</sup> 

<sup>1</sup>Department of Respiratory Medicine, The First Affiliated Hospital of Weifang Medical University/Weifang People's Hospital, Weifang, 261000, People's Republic of China; <sup>2</sup>School of Clinical Medicine, Weifang Medical University, Weifang, 261053, People's Republic of China; <sup>3</sup>Department of Laboratory Medicine, The First Affiliated Hospital of Weifang Medical University/Weifang People's Hospital, Weifang, 261000, People's Republic of China

\*These authors contributed equally to this work

Correspondence: Wei Tan, Department of Respiratory Medicine, Weifang People's Hospital, 151 Guangwen Street, Weifang, Shandong Province, 261000, People's Republic of China, Email 13863659099@126.com; Xue Zhao, Department of Laboratory Medicine, Weifang People's Hospital, 151 Guangwen Street, Weifang, Shandong Province, 261000, People's Republic of China, Email 42281870@qq.com

**Purpose:** Owing to its noninvasive nature, broad-spectrum effectiveness, minimal bacterial resistance, and high efficiency, phototherapy has significant potential for antibiotic-free antibacterial interventions and combating antibacterial biofilms. However, finding effective strategies to mitigate the detrimental effects of excessive temperature and elevated concentrations of reactive oxygen species (ROS) remains a pressing issue that requires immediate attention.

**Methods:** In this study, we designed a pH-responsive cationic polymer sodium nitroside dihydrate/branched polyethylenimine-indocyanine green@polyethylene glycol (SNP/PEI-ICG@PEG) nanoplatform using the electrostatic adsorption method and Schiff's base reaction. Relevant testing techniques were applied to characterize and analyze SNP/PEI-ICG@PEG, proving the successful synthesis of the nanomaterials. In vivo and in vitro experiments were performed to evaluate the antimicrobial properties of SNP/PEI-ICG@PEG.

**Results:** The morphology and particle size of SNP/PEI-ICG@PEG were observed via TEM. The zeta potential and UV-visible (UV-vis) results indicated the synthesis of the nanomaterials. The negligible cytotoxicity of up to 1 mg/mL of SNP/PEI-ICG@PEG in the presence or absence of light demonstrated its biosafety. Systematic in vivo and in vitro antimicrobial assays confirmed that SNP/PEI-ICG@PEG had good water solubility and biosafety and could be activated by near-infrared (NIR) light and synergistically treated using four therapeutic modes, photodynamic therapy (PDT), gaseous therapy (GT), mild photothermal therapy (PTT, 46 °C), and cation. Ultimately, the development of Gram-positive ( $G^+$ ) *Staphylococcus aureus* (*S. aureus*) and Gram-negative ( $G^-$ ) *Escherichia coli* (*E. coli*) were both completely killed in the free state, and the biofilm that had formed was eliminated.

**Conclusion:** SNP/PEI-ICG@PEG demonstrated remarkable efficacy in achieving controlled multimodal synergistic antibacterial activity and biofilm infection treatment. The nanoplatform thus holds promise for future clinical applications.

**Keywords:** cationic, mild photothermal, photodynamic, NO gas, antibacterial

## Introduction

Bacteria have coevolved with humans in symbiotic relationship based on mutual dependence.<sup>1-3</sup> When the human immune system is compromised due to factors such as exposure to cold temperatures, fatigue, or illnesses, the probability of bacterial infection significantly increases. The severity of infection primarily relies on the virulence of bacteria and may involve biofilm formation. Biofilms, as umbrellas for free-living bacteria, are microcommunities of large number of free-living bacteria encapsulated in the extracellular polymeric substance (EPS) they produce. Biofilms tend to resist the

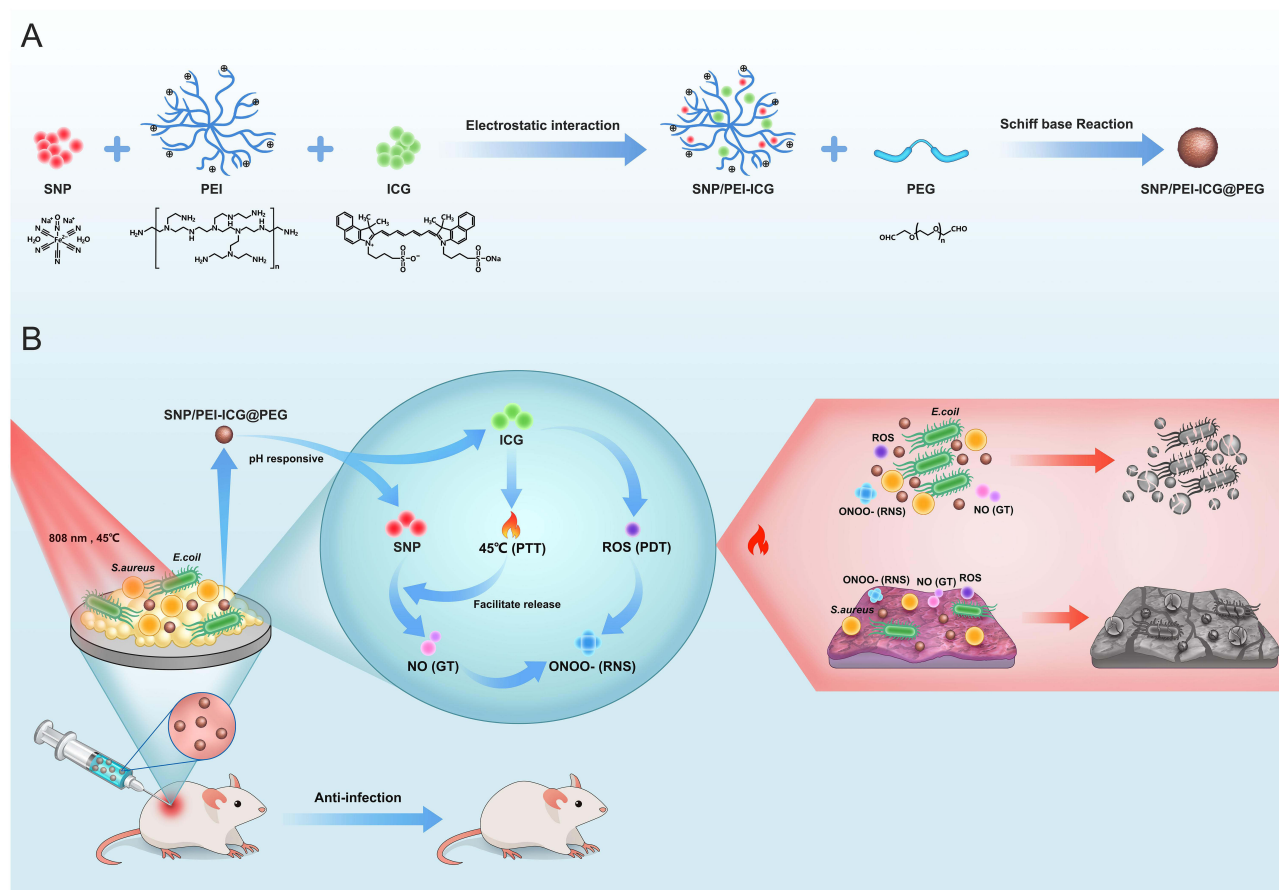
host's immune system, reduce antibiotic susceptibility, and impede antibiotic leakage, making them difficult to treat. Biofilms have been reported to be up to 1,000 times more resistant to antibiotics than bacteria in the free state.<sup>3-6</sup> The presence of biofilms, the development of bacterial resistance, and the long lead time for new antibiotic development make it necessary to reduce the overreliance on antibiotics.<sup>7,8</sup> Efforts to develop new antimicrobial agents that are less prone to resistance and have effective bactericidal properties are important for advancing future antimicrobial research.

With the progress of nanomedicine, an increasing number of nanomaterials and innovative antibacterial therapies have been employed for antibacterial treatment research. Previously investigated nanomaterials include precious metal nanoparticles, carbon-based nanomaterials, organic small-molecule nanomaterials, and polymer-based nanomaterials. Phototherapy, gas therapy, sonodynamic therapy, cold atmospheric plasma therapy and chemical dynamic therapy are among the emerging antibacterial approaches.<sup>9-11</sup> Compared to other modalities, phototherapy is garnering attention due to advantages such as broad spectrum coverage, non-invasiveness, deep tissue penetration and evasion of drug resistance. Photodynamic therapy (PDT) has been extensively applied in the clinical treatment of infectious diseases. Superior photosensitizers (PSs) can convert light energy into heat energy under NIR stimulation leading to cell membrane rupture, protein denaturation, and subsequently bacterial death. They can also transfer absorbed energy to molecular oxygen for generating cytotoxic ROS, which can oxidize and destroy biological molecules such as lipids, proteins, and nucleic acids, thereby inducing bacterial death.<sup>12,13</sup> It has been reported that the combination of PDT and PTT exhibits effective bactericidal and biofilm elimination capabilities; however, the high temperatures (> 50 °C) associated with the application of these therapies may cause damage to normal cells.<sup>14</sup> Thus, it is imperative to cautiously explore the combination of mild PTT and other therapeutic approaches for the sterilization and eradication of biofilms.<sup>15</sup>

Gaseous therapy (GT) is increasingly used in combination with other therapies because gas molecules are non-inductive of drug resistance, have favorable biosafety profiles, and are important endogenous signaling molecules in vivo. Five representative gas molecules have been identified: hydrogen (H<sub>2</sub>), nitric oxide (NO), sulfur dioxide (SO<sub>2</sub>), hydrogen sulfide (H<sub>2</sub>S), and carbon monoxide (CO).<sup>16,17</sup> Among these, NO is widely distributed in various tissues of organisms, where it regulates physiological processes such as blood vessel growth, immune response modulation, and cell apoptosis. Research in the biomedical field has shown that low concentrations (<1 μM) of NO can promote wound healing while high concentrations (>1 μM) induce oxidative stress-mediated protein, DNA denaturation, and cell membrane rupture, effectively eliminating bacteria.<sup>18-20</sup> Furthermore, NO exhibits biofilm-dispersing properties by interfering with nucleotide signals such as c-di-AMP and c-di-GMP.<sup>21</sup> In serving as an adjunct therapy to enhance mainstream treatments such as PDT, NO reacts with the ROS generated during PDT to produce highly lethal peroxynitrite (ONOO<sup>-</sup>) species that are more effective against bacteria than NO alone.<sup>22,23</sup> Despite the numerous advantages of NO in antimicrobial therapy applications, its volatility, explosive release, and short half-life are significant challenges that necessitate the development of nanomaterials capable of stable storage and of stimulating the on-demand release of NO.<sup>24</sup>

To address these issues, we constructed cationic SNP/PEI-ICG@PEG nanoparticles that could target bacteria with excellent biosafety and photostability and could thus be utilized as treatment platform for multiple antibacterial modes, including mild PTT, PDT and controlled NO release under 808 nm laser irradiation (Scheme 1). The cationic polymer PEI was employed as a cross-linker, facilitating the successive introduction of negatively charged SNP and ICG through electrostatic interactions to form the core of SNP/PEI-ICG nanospheres. Subsequently, the Schiff base reaction between aldehyde-modified PEG and the amino groups on the surfaces of the SNP/PEI-ICG nanospheres was utilized for PEGylation, which effectively enhanced the stability and water solubility of the nanospheres. Consequently, a robust and efficient nanomedicine platform was constructed.

As an endogenous gaseous signalling molecule, NO is involved in important physiological and pathological processes, and its potential for the treatment of cancer, bacterial infections, and wound healing is particularly of interest. NO not only could kill bacteria through various processes, including membrane damage, DNA cleavage, and bacterial metabolic dysfunction, but also inhibits the spread of biofilm and trigger the immune system's response to infection. However, how to accurately transport NO gas to bacterial biofilms on demand and at a fixed point is a scientific problem that researchers are concerned about and need to solve. The particles designed by us, with smaller size, greater positive surface charge, and higher surface density of NO donors, generally exhibit improved antimicrobial activity. This



**Scheme 1** pH-responsive cationic SNP/ICG-PEI@PEG polymers. **(A)** Preparation method; **(B)** principle of application in antimicrobial therapy.

improvement can be attributed to faster association with bacteria, greater penetration into biofilms, and more efficient delivery of NO.

Cationic SNP/PEI-ICG@PEG nanoparticles can capture bacteria through electrostatic interactions, disrupting the cell membrane and enhancing its permeability.<sup>25,26</sup> Under weak acidic conditions, the acid-sensitive Schiff base bond in SNP/PEI-ICG@PEG is cleaved, leading to the release of the core component of the nanosphere.<sup>27</sup> Under NIR irradiation, SNP/PEI-ICG@PEG promotes mild photoheating and ROS generation by ICG while simultaneously preventing ICG quenching through PEI scaffold-induced molecular spacing.<sup>28,29</sup> Additionally, SNP facilitates Fe-NO coordination bond cleavage upon photothermal stimulation, resulting in free NO production and increased antimicrobial susceptibility.<sup>30</sup> The nanoparticles demonstrated exceptional phototherapy and controlled NO release properties as well as efficient synergistic antibacterial and antibiofilm effects in our in vitro and in vivo experiments. The development of these nanoparticles opens up promising prospects for the clinical translation of nanomedicine.

## Materials, Characterization and the Synthesis of SNP-ICG/PEI@PEG Nanoparticles (NPs)

### Materials

Indocyanine green (ICG) was purchased from Maclean Biochemical Technology Co. Ltd (99%, Shanghai, China). Branched polyethylenimine (PEI, 25 kDa) and PEG (2 kDa) were supplied by Sigma-Aldrich (Sunnyvale, CA, USA).  $\text{Na}_2[\text{Fe}(\text{CN})_5\text{NO}]\cdot 2\text{H}_2\text{O}$  (SNP) was obtained from Aladdin Industry Corporation (Shanghai, China). Further, 1,3-diphenylisobenzofuran (DPBF) was purchased from Shanghai D&B Biology Science and Technology Co., Ltd, and 2,3,5-triphenyl-2H-tetrazolium chloride (TTC) and crystal violet (CV) were purchased from Beijing Solarbio Science &

Technology Co., Ltd. A nitric oxide assay kit was obtained from Beyotime Biotechnology (Shanghai, China), and a Live/Dead Bacterial Staining Kit was supplied by the Yeasen Corporation (Shanghai, China). All chemicals were directly used without further purification. Standard strains of *E. coli* (ATCC 25922) and *S. aureus* (ATCC 6538) were procured from Forhigh Biotech Co., Ltd. (Hangzhou, China).

### Synthesis of SNP-ICG/PEI@PEG NPs

Equal specific gravity (1:1, 20 mg) SNP and PEI were dissolved simultaneously in distilled water (5 mL) and the beaker containing the mixture was placed on a magnetic stirrer for 4 h of continuous stirring. The mixture was then centrifuged at 10,000 rpm for 10 min and washed three times with distilled water. ICG (5 mg) was dissolved in distilled water (5 mL) and slowly added to the polymer precipitation obtained through the above steps using a rubber-tipped burette. The mixture was stirred on a magnetic stirrer for 8 h, centrifuged at 10,000 rpm for 10 min, and washed three times with distilled water resulting in SNP/PEI-ICG NPs.

The precipitate obtained was dispersed in 5 mL of distilled water, with aldehyde-modified PEG (80 mg) slowly added during the mediation process, mixed, centrifuged at 10,000 rpm for 10 min, and washed three times with distilled water. The final precipitate was kept in a freeze dryer. The dark green powder obtained was SNP/PEI-ICG@PEG NPs.

### Characterization

A 15  $\mu$ L solution of the nanomaterials was added dropwise onto a copper mesh. After leaving it to dry naturally, the particle size and morphology of the nanomaterials were characterized via TEM (Tecnai G2 20 TWIN, FEI, US). The zeta potentials of the samples were measured using a Zetasizer (Nano ZSP, Malvern, UK). The absorption wavelengths of ICG, SNP, and the SNP-PEI-ICG@PEG NPs were measured using a UV-Vis spectrophotometer (T6 New Century, Beijing Persee General Instrument Co., Ltd., China).

## Methods

### Physical and Chemical Properties of Nanomaterials

#### Standard Curve of ICG

ICG green powder was dissolved in pure water to obtain ICG solutions of different concentrations of ICG solutions (1.25, 2.5, 5.0, 10, and 20  $\mu$ g/mL in a solution volume of 2 mL). The configured ICG solutions were placed in a quartz dish and UV-vis spectroscopy was applied to determine the absorbance levels of the ICG solutions at 778 nm. The obtained data were used to plot a linear fitting graph on GraphPad 8.0 software.

#### ICG Drug Loading Rate

In the first step, SNP (1.6 mg) was added to PEI solution (2 mg/mL, 1.6 mg) and stirred continuously for 4 h in the dark. Centrifugation was performed at 10,000 rpm for 10 min. The precipitate was rinsed with pure water to clarify the supernatant.

In the second step, the obtained precipitate was dissolved in 1 mL of pure water, to which ICG (400  $\mu$ g) was added and stirred continuously for 8 h in the dark. Centrifugation was performed at 10,000 rpm for 10 min. The supernatant obtained was subjected to UV-vis spectroscopy to determine the absorbance at 778 nm and subsequently the ICG loading rate was calculated using the following formula:

$$\text{ICG drug loading rate(\%)} = (W_1 - W_2) / W_3 \times 100\%$$

$W_1$  refers to the total amount of ICG added,  $W_2$  is the free ICG in suspension, and  $W_3$  is the weight of the final SNP/PEI-ICG@PEG complex.

### Generation of ROS

DPBF has been extensively used in measuring single-linear state oxygen ( $^1\text{O}_2$ ) generation to evaluate the photodynamic properties of nanomaterials. 2 mL dimethyl sulfoxide (DMSO) was added to a cuvette as a base solution. DPBF solution (1 mg/mL, 20  $\mu$ L) was mixed with an aqueous solution of SNP/PEI-ICG@PEG NPs (50  $\mu$ g/mL, 500  $\mu$ L) in the cuvette. Continuous NIR irradiation of 808 nm was performed with different laser powers (0.4, 0.8, 1.0, 1.6  $\text{W}/\text{cm}^2$ ), and the

absorption spectra and absorbance at 418 nm of the different treatment groups were determined using a UV-vis spectrophotometer.

## Photothermal Performance of SNP/PEI-ICG@PEG NPs

A 200  $\mu\text{L}$  aqueous solution of SNP/PEI-ICG@PEG NPs with different concentrations (0, 112.5, 225, 450 and 1000  $\mu\text{g}/\text{mL}$ , PBS) were added to each hole of a 96-well plate and irradiated using an 808 nm laser. The temperature of the solution was monitored using FLIR Tools (ETS320, FLIR, USA), a PTT monitoring system.

## Determination of NO Production

A centrifuge tube containing SNP/PEI-ICG@PEG aqueous solution (1 mg/mL, 1 mL) was irradiated with an 808 nm laser (1.0 W/cm<sup>2</sup>). Subsequently, centrifugation was performed at 10,000 rpm for 10 min. The Griess reagent method was used to determine the NO content.

## In vitro Experiments

### Bacterial Culture

*E. coli* and *S. aureus* on blood agar plates were transferred to 4 mL of liquid Luria–Bertani (LB) culture medium and cultured for 18 h in a shaking incubator at 37 °C under 120 rpm rotation. The bacteria were diluted with the liquid LB culture medium for further use until the OD at 600 nm reached 0.1.

### In vitro Antibacterial Assays

The minimum inhibitory concentration (MIC) and minimum bactericidal concentration (MBC) are important indexes to evaluate the antibacterial performance of antibacterial drugs. We used the microbroth dilution method to determine the MIC of the drug against microbiology. Using the multiplicative dilution method, equal volumes of TTC solution and SNP/PEI-ICG@PEG solution were thoroughly mixed (solvent: Luria-Bertani (LB) broth, volume: 50  $\mu\text{L}$ , TTC solution concentration: 5 mg/mL). The SNP/PEI-ICG@PEG mixture was configured into different concentration gradients (0.22–900  $\mu\text{g}/\text{mL}$ ) and bacterial solution (100  $\mu\text{L}$ ,  $1 \times 10^6$  CFU/mL) was thoroughly mixed with the configured mixing solutions, respectively. This was then incubated for 30 min at 37 °C. The above NPs were divided into three groups for testing: SNP + Laser, SNP/PEI-ICG@PEG + Laser, and SNP/PEI-ICG@PEG + Laser + cooling. Each test hole was irradiated at 808nm for 5 min using a 1.0 W/cm<sup>2</sup> laser. The SNP/PEI-ICG@PEG + Laser + cooling group was placed on an ice bath to control the temperature increase during the operation. Following incubation at 37 °C for 24 h, the color changes and turbidity of each experimental group were observed, and the optical density (OD) values at 600 nm were measured with an enzyme marker to calculate the MIC.

After blowing and mixing the MIC,  $2 \times \text{MIC}$  and  $4 \times \text{MIC}$  pore bacterial solutions, 75  $\mu\text{L}$  of each solution was pipetted out and applied to a blood plate, which was then placed in an incubator at 37 °C for 24 h. The MBC was determined based on the number of individual colonies on the blood plate.

### Plate Count

The antibacterial activity of SNP/PEI-ICG@PEG was evaluated on blood agar plates. Bacteria ( $1.0 \times 10^6$  CFU/mL) were mixed with SNP/PEI-ICG@PEG suspension and incubated at 37 °C for 30 min. The reaction solution was irradiated with laser (808 nm, 1.0 W/cm<sup>2</sup>) for 5 min. Incubated at 37 °C for 12 h, the reaction solution was diluted 1000 times with PBS, and 60  $\mu\text{L}$  was applied to the blood agar plates. Incubated at 37 °C overnight and counted by Image J software. Bacterial activity was calculated by comparing the CFU number of the sample with that of the control group (normal saline). The effects of different concentrations of SNP/PEI-ICG@PEG on antimicrobial performance were studied in the range of 112.5–450  $\mu\text{g}/\text{mL}$ .

### Live/Dead Bacteria Staining Assay

We stained the different treatment groups according to the prescribed process for using the Bacterial Live/Dead Staining Kit. The results were observed under an inverted fluorescence microscope, and the fluorescence intensities of the pictures were quantitatively analyzed.

## Transmission Electron Microscopy of Bacteria

The bacterial solution of *S. aureus* or *E. coli* were treated as described above. Bacterial cells were fixed with 2.5% glutaraldehyde solution (4 °C, 24 h), washed three times with PBS, embedded in agar, and blocked. The bacteria were then dehydrated by sequential treatment of ethanol solutions (30%, 50%, 70%, 90%, 95%, and 100%) for 10 min each at room temperature, followed by dealcoholization with acetone for 3 h at room temperature, embedding by gradient penetration of the embedding medium, negative staining, and sectioning on a nickel mesh for TEM observation.

## Formation of Biofilms

*S. aureus* suspension (500  $\mu\text{L}$ ,  $1 \times 10^8$  CFU/mL) was blended well with LB broth (500  $\mu\text{L}$ ) and added to a 24-well plate, which was then incubated at 37°C for 24 h. The aged LB broth was replaced with to fresh broth, and the biofilm was incubated for another 24 h. Finally, the *S. aureus* biofilm attached to the 24-well plate was harvested. The same method was used to prepare *E. coli* biofilms.

## Elimination of the Formed Biofilm

After preparation of the biofilm, the aged LB broth was slowly sucked out using a 1 mL syringe, and then the aqueous solution (SNP and SNP/PEI-ICG@PEG, at the concentrations of 450  $\mu\text{g}/\text{mL}$ ) was added into each well, and PBS was added to the control sample. After 30 min of incubation, the biofilms were irradiated with laser (808 nm, 1.0 W/cm<sup>2</sup>, 5 min). The “SNP/PEI-ICG@PEG + Laser + cooling” group was placed on an ice bath for treatment, and the temperature was controlled. After treatment, each well was cleaned with PBS three times, and 500  $\mu\text{L}$  of methanol was added and fixed for 30 min. The solution was then discarded. After air drying, 0.5% CV of 200  $\mu\text{L}/\text{well}$  was added and dyed for 30min. They were then cleaned three times and observed under an inverted fluorescence microscope. After filming, the biofilm was dissolved with ethanol, and the absorbance of OD<sub>570</sub> was measured.

## Hemolytic Test

The blood compatibility of SNP/PEI-ICG@PEG was determined spectrophotometrically based on the principle that heme released from ruptured erythrocytes has maximum absorption in the visible wavelength band. First, an appropriate amount of fresh blood from mice was taken and centrifuged in a centrifuge (2000 rpm, 10 min) to separate the erythrocytes from whole blood, and then scrubbed with PBS three times and diluted to 4.0%. PBS and water were set up as negative and positive control groups, respectively, and SNP/PEI-ICG@PEG suspensions with different concentrations (125, 250, 500 and 1000  $\mu\text{g}/\text{mL}$ ) were set up as experimental groups which were treated with erythrocytes at the same time.

Finally, the solutions of each group were centrifuged after 3 h of reaction in an incubator at 37 °C. The supernatants were placed in the microtiter wells of a 96-well plate and their absorbance at 540 nm was measured. The hemolysis rate was determined by the following equation (Equation 1):

$$\text{Hemolysis ratio(\%)} = \frac{A_{(\text{sample})} - A_{(\text{negative})}}{A_{(\text{Water})} - A_{(\text{negative})}} * 100\% \quad (1)$$

## Cell Lines and Cell Culture

The mouse epithelial-like fibroblasts L929 were observed from American type culture collection (ATCC). L929 cells were grown in culture medium of 10% fetal bovine serum (FBS), 1% antibiotics and 89% RPMI 1640 medium in a humidified incubator at 37 °C with 5% CO<sub>2</sub>.

## In vitro Cytotoxicity Assay

The effect of SNP/PEI-ICG@PEG on the viability of L929 cells was assessed by MTT assay. Logarithmically amplified L929 cells were placed in 96-well plates ( $5 \times 10^4/\text{well}$ ) and cultured for 24 h. The medium was removed and different concentrations of SNP/PEI-ICG@PEG solutions (0, 125, 250, 500, 1000  $\mu\text{g}/\text{mL}$ ) were added and incubated for 24 h. After discarding the supernatant, an equal amount of RPMI 1640 medium was added. Then, 15  $\mu\text{L}$  MTT solution

(5 mg/mL) was added. After 4 h, the solution was removed and subsequently 120  $\mu$ L/well of DMSO solution was added to eventually produce water-insoluble blue-purple crystalline Formazan. The absorbance (Abs) of each well at 490 nm was measured using an enzyme marker (BioTek Instruments, USA).

The cytotoxicity test procedures of SNP and “SNP/PEI-ICG@PEG + Laser” are the same as above.

## In vivo Antibacterial and Wound Healing Evaluation of SNP/PEI-ICG@PEG NPs

### Animals

Female KM mice (6 weeks of age) were obtained from Jinan Pengyue Experimental animal Breeding Co., Ltd. (Jinan, China). The animal experiments were performed in accordance with the rules of the Animal Experiment Ethics Committee of Weifang Medical University. The mice were anesthetized, and skin incisions of approximately 8 mm in diameter were created on their backs using surgical instruments. The mice were then titrated with *S. aureus* for two days.

## Evaluation of in vivo Synergistic Antibacterial Activity

After two days of bacterial infection, the mice were randomly divided into five groups: PBS + laser, SNP/PEI-ICG@PEG, SNP + laser, SNP/PEI-ICG@PEG + laser + cooling, SNP/PEI-ICG@PEG + laser. The concentrations of the drug solutions were all 450  $\mu$ g/mL. The solutions were carefully sprayed on the wound surface and then irradiated with laser (1.0 W/cm<sup>2</sup>, 5 min). During the treatment period, the weight of the mice was measured and photographs of the wounds were taken. On the last day, the mice were tested for blood, vital organs, and skin tissues around the wounds.

## Statistical Analysis

All experiments were repeated more than 3 times. Data were analysed using GraphPad Prism (version 8.0), Origin 2019b and Image J software. The mean  $\pm$  standard deviation (mean  $\pm$  SD) was calculated. Differences in results were compared using *t*-test and one-way analysis of variance (ANOVA). (Statistically significant when *p*-value < 0.05. The smaller the *p*-value the greater the significance. \**p* < 0.05, \*\**p* < 0.01, \*\*\**p* < 0.001, \*\*\*\**p* < 0.0001).

## Results and Discussion

### Characterization of Various Nanoparticles

PEI is widely used in gene carrier research due to its large number of cations and “proton sponge effect”. The greater the number of amine groups with different degrees of branching in PEI molecules, the higher molecules’ protonation ability and charge density, the stronger their affinity for cells and the greater their cytotoxicity.<sup>30,31</sup> Many studies have utilized the properties of polyethylene glycol such as low toxicity, hydrophilicity, and easy chemical modification. The combination of PEG and PEI is known as polyethylene glycol PEI. This combination reduces the positive charge and aggregation susceptibility of PEI and increases its stability.<sup>32,33</sup>

In the present study, the positive charge property of PEI was utilized to attract SNP and ICG and encapsulate them in polyethylene glycolized PEI. TEM showed that the resulting SNP/PEI-ICG@PEG was observed to be a uniformly sized spherical structure in pure water at pH 7.4 with a measured particle size of 51.64  $\pm$  11.14 nm. The presence of PEI also helped maintain the distance between ICG molecules, preventing fluorescence burst. However, when SNP/PEI-ICG@PEG was left in pure water at pH 6.0 for 2 h, it underwent cleavage, and the particle size was reduced to 6.8  $\pm$  2.38 nm. This confirmed that the NPs fractured the Schiff base bond in the acidic environment, resulting in SNP and ICG being released from the protected interior and subjected to laser irradiation, enabling them to play their roles in antibacterial (Figure 1A–C). SNP/PEI-ICG@PEG was cultured in PBS, and the particle size of NPs at different time periods (0, 2, 4, 6, 12, 24, 48 h) was continuously determined by dynamic light scattering (DLS). Obviously, the particle size of SNP/PEI-ICG@PEG did not change much within 24 h, indicating the stability of NPs, which is conducive to maintain stability on the skin wound surface. However, the particle size results of DLS are slightly larger than those of TEM, considering the substances absorbed on the surface of NPs when measured with DLS (Figure 1D).<sup>34</sup> To further verify successful nanomaterial synthesis, we conducted zeta potential testing with various materials (Figure 1E). SNP/PEI exhibited a negative charge with a zeta potential of 20.67  $\pm$  0.51 mv, which decreased to -5.21  $\pm$  0.18 mv upon combination with

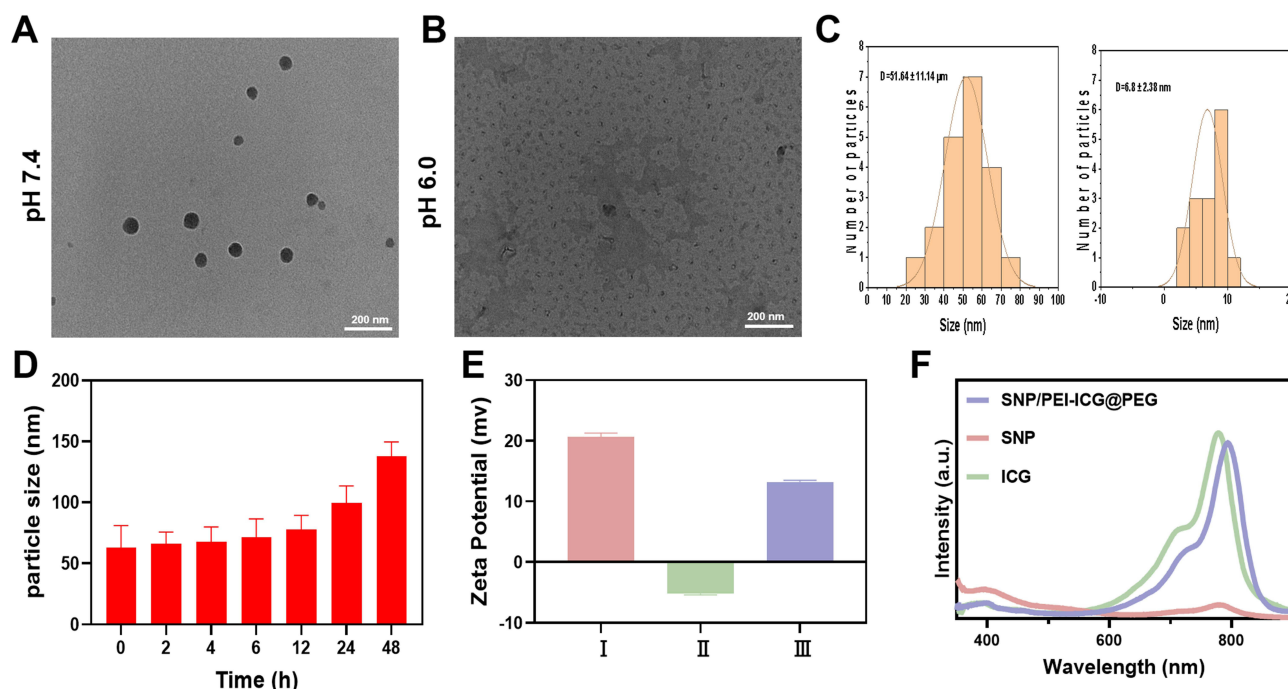


**Figure 1** (A) TEM image of SNP/PEI-ICG@PEG dispersion in pure water at pH 7.4 (concentration: 450  $\mu\text{g}/\text{mL}$ ); (B) TEM image of SNP/PEI-ICG@PEG after standing in pure water (concentration: 450  $\mu\text{g}/\text{mL}$ ) at pH 6.0 for 2 h; (C) TEM images were obtained using the corresponding particle size profile determined by Image J; (D) Particle size of SNP/PEI-ICG@PEG at different time periods (0, 2, 4, 6, 12, 24, 48 h) determined by DLS (culture solvent: PBS, concentration: 450  $\mu\text{g}/\text{mL}$ ); (E) zeta potentials of SNP/PEI (I), SNP/PEI-ICG (II), and SNP/PEI-ICG@PEG (III); (F) UV-vis spectra of SNP, ICG, and SNP/PEI-ICG@PEG (The solution concentrations were SNP 1.5 mg/mL, ICG 5  $\mu\text{g}/\text{mL}$ , SNP/PEI-ICG@PEG 3.0 mg/mL, respectively).

the negatively charged ICG (ie, SNP/PEI-ICG) and subsequently increased to  $13.22 \pm 0.22$  mv after being coated with PEG (ie, SNP/PEI-ICG@PEG). The consistent alteration in zeta potential indicates the gradual binding of each monomer under the influence of electrostatic forces.

From the UV-vis spectra of the various nanomaterials (Figure 1F), we observed that the primary absorption peaks were at 392 nm and 770 nm for SNP and at 392 and 778 nm for ICG. In the case of SNP/PEI-ICG@PEG, the absorption peaks for each monomer merged in the spectra and were distributed at wavelengths of 399 and 794 nm. Notably, Li et al and Zhang et al reported that PEI and PEG have no significant UV absorption peaks.<sup>35,36</sup> A red shift was observed at 700–800 nm for SNP/PEI-ICG@PEG, which could be attributed to the strong binding of ICG within the polymer core. The presence of an absorption peak near 808 nm for SNP/PEI-ICG@PEG confirmed its potential for both PTT and PDT upon laser excitation at this wavelength. A 700–950 nm NIR light source has previously been reported as optimal for PTT because it leads to enhanced tissue penetration and reduced absorption by surrounding tissues.<sup>37,38</sup> Therefore, we used an 808 nm laser for subsequent experimental investigations. ICG is a photosensitizer that generates ROS and undergoes photothermal conversion after being triggered by 808 nm laser light, playing a role in the release of NO and the generation of ROS. Thus, we determined the standard curve equation for ICG to be  $y=0.1270x - 0.07742$ . The calculated load factor was 11.50% (Figure S1; Table S1).

## Evaluation of Photothermal, NO Release and Photodynamic Performance

The photothermal performance of SNP/PEI-ICG@PEG was assessed under various conditions to identify the optimal parameters for achieving mild photothermal temperatures. The aqueous solution of SNP/PEI-ICG@PEG demonstrated a concentration-dependent temperature change upon irradiation with the same laser (808 nm, 1.0 W/cm<sup>2</sup>, 5 min), as illustrated in Figure 2A.

After NIR irradiation, the temperature of PBS increased from 25.5 °C to 28.6 °C, with a temperature change ( $\Delta T$ ) of only 2.8 °C. However, when the SNP/PEI-ICG@PEG dispersion with a concentration of 450  $\mu\text{g}/\text{mL}$  received the same NIR irradiation, the  $\Delta T$  by 20.6 °C from 25.5 °C to 46.1 °C. Furthermore, when a constant concentration of SNP/PEI-



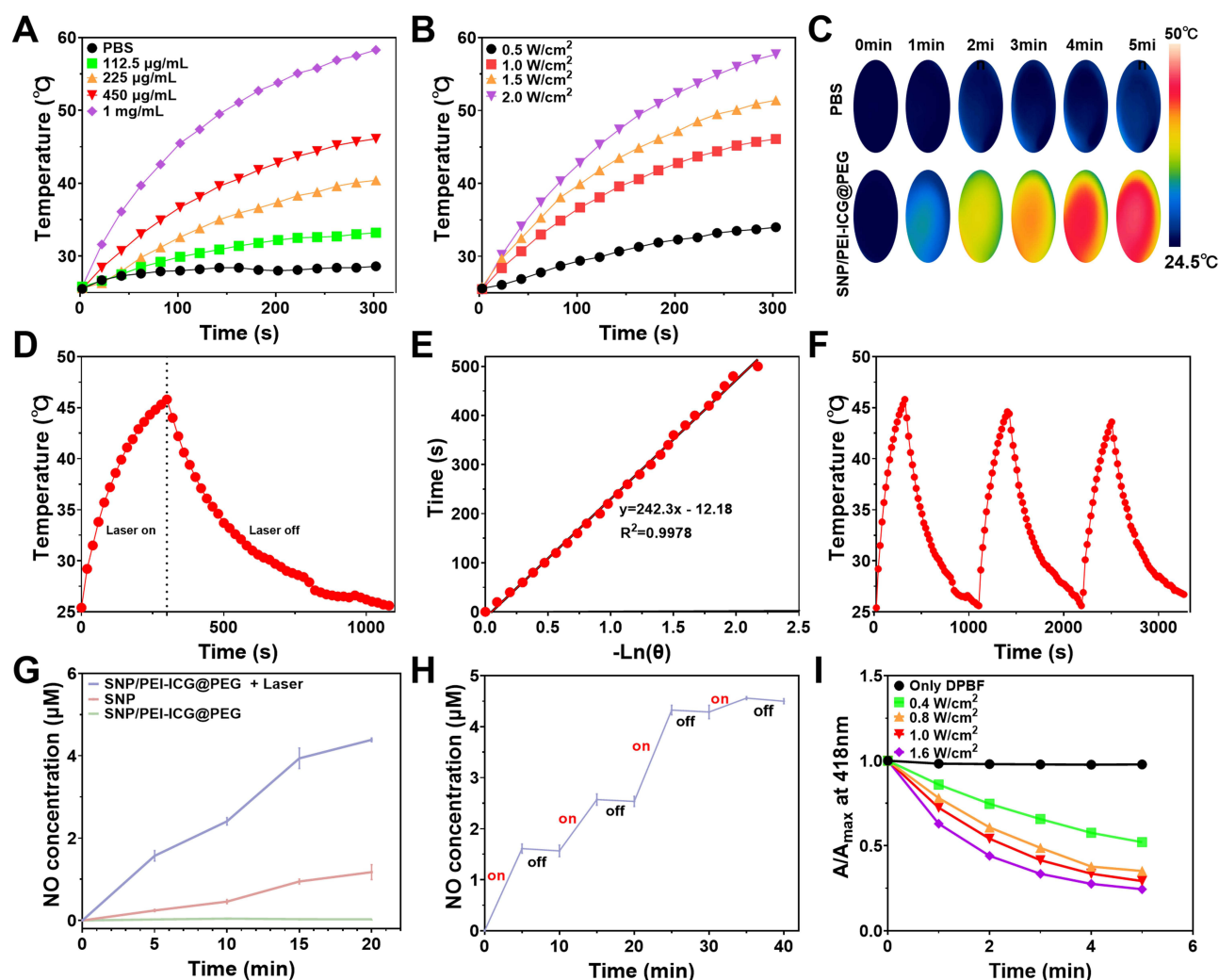


**Figure 2** (A) Concentration-dependent temperature change of the SNP/PEI-ICG@PEG solution after exposure to NIR irradiation ( $1.0 \text{ W/cm}^2$ , 5 min; concentration: 112.5, 225, 450, 1000  $\mu\text{g/mL}$ ); (B) power-dependent temperature change of 450  $\mu\text{g/mL}$  SNP/PEI-ICG@PEG solution under irradiation; (C) infrared thermal imaging of PBS and SNP/PEI-ICG@PEG solutions (450  $\mu\text{g/mL}$ ) under NIR irradiation ( $1.0 \text{ W/cm}^2$ , 5 min); (D) temperature change curves for the SNP/PEI-ICG@PEG solution (450  $\mu\text{g/mL}$ ,  $1.0 \text{ W/cm}^2$ ) under NIR irradiation and after switching off the laser switching; (E) the cooling time plot versus negative natural logarithm of driving force temperature ( $-\ln(\theta)$ ) with  $\tau_s = 242.3$  and a concentration of 450  $\mu\text{g/mL}$ ; (F) photothermal cycle curve of the SNP/PEI-ICG@PEG solution (450  $\mu\text{g/mL}$ ,  $1.0 \text{ W/cm}^2$ ) in the third open-concern cycle under NIR irradiation; (G) NO release from SNP/PEI-ICG@PEG without NIR irradiation and SNP and SNP/PEI-ICG@PEG with NIR irradiation (all sample concentrations adjusted to 1 mg/mL) ( $1.0 \text{ W/cm}^2$ ); (H) the “on–off” release behavior of SNP/PEI-ICG@PEG (1 mg/mL) under NIR irradiation ( $1.0 \text{ W/cm}^2$ ); (I) UV absorption changes of DPBF at 418 nm only under irradiation of SNP/PEI-ICG@PEG cocultured with NIR ( $1.0 \text{ W/cm}^2$ ) and DPBF at different NIR powers (0.4, 0.8, 1.0, and 1.6  $\text{W/cm}^2$ ).

ICG@PEG solution was maintained (450  $\mu\text{g/mL}$ ), there was a positive correlation between the temperature change and laser power (Figure 2B) thermal imaging (Figure 2C), revealed that the color of the SNP/PEI-ICG@PEG solution was dark red when it heated up, whereas PBS remained its original dark blue hue, resulting in an obvious color contrast. To quantify the photothermal conversion efficiency ( $\eta$ ) of the nanoparticles, we determined the temperature change curves for the SNP/PEI-ICG@PEG solution (450  $\mu\text{g/mL}$ ) during both heating and cooling processes. From these curves (Figure 2D), we calculated the corresponding thermal time constant ( $\tau_s$ , Figure 2E) and derived a  $\eta$  value of 18.59%. SNP/PEI-ICG@PEG not only exhibited good photothermal properties but also showed negligible changes in the temperature profile after three cycles of repeated photothermal-cooling, indicating its excellent photostability (Figure 2F).

To evaluate whether SNP/PEI-ICG@PEG could accomplish controllable NO release and its ability to release NO under NIR irradiation, we quantitatively monitored NO release using a Griess reagent assay; the release amount of NO was calculated with the help of the standard curve given in Figure S2.<sup>39</sup> As shown in Figure 2G, SNP exhibited minimal NO generation upon irradiation, while the SNP/PEI-ICG@PEG formulations showed negligible NO release after dark

treatment. Conversely, the amount of NO released by SNP/PEI-ICG@PEG when triggered by the 808 nm laser increased proportionally with the duration of irradiation. These results confirmed that SNP/PEI-ICG@PEG rapidly accomplished photo-thermal conversion upon NIR irradiation, accelerated the breakage of the Fe–NO ligand bond, and significantly augmented the NO release rate. To further verify the direct relationship between NO release and laser irradiation, we used intermittent laser irradiation with SNP/PEI-ICG@PEG and plotted the “on–off” control curves of NO (Figure 2H). The results showed that the amount of NO production was almost zero when the laser was turned off, and a relatively stable release rate of NO occurred during laser irradiation, suggesting that the release of nitric oxide can be further enhanced by the photothermal effect.<sup>40</sup> This fully demonstrated that the release of NO from SNP/PEI-ICG@PEG can be precisely controlled using an 808 nm NIR laser, which is conducive to its precise anti-inflammatory effect at the site of bacterial infection in vivo.

According to the literature, 1,3-diphenylisobenzofuran (DPBF) can bind to and react highly specifically with single-linear oxygen, which causes a decrease in its characteristic UV absorption peak and determines the generation of ROS (Figure 2I, Figures S3).<sup>41</sup> When a solution of SNP/PEI-ICG@PEG was introduced to DPBF solution, the characteristic peak of the mixture emerged at 808 nm under a laser (1.0 W/cm<sup>2</sup>), and the absorbance exhibited a continuous decline over time, with an approximate reduction of 76% in 5 min. In contrast, when DPBF solution alone was subjected to illumination, there was a negligible change in absorbance. These observations confirmed the production of ROS and the positive correlation between the ROS production rate and laser power. The above experiments clarified that SNP/PEI-ICG@PEG could effectively generate toxic ROS by PDT, and that PTT triggered NO generation and enhanced the PDT effect.

In sum, SNP/PEI-ICG@PEG can produce a mild photothermal effect and ROS exhibiting bacterial toxicity under laser irradiation, triggering the release of NO in a controlled manner. This method of synergistic PTT/PDT/GT treatment raises the possibility of safe and efficient antimicrobial therapy.

## Antibacterial Experiment in vitro

The excellent material properties of SNP/PEI-ICG@PEG motivated us to completely determine the in vitro antimicrobial properties of its system. SNP/PEI-ICG@PEG is theoretically a broad-spectrum antimicrobial agent; therefore, we decided to perform antimicrobial treatments against *S. aureus* (G<sup>+</sup>) and the *E. coli* (G<sup>-</sup>).

First, we determined the MIC and MBC levels of the nanomaterials against the two types of bacteria.<sup>42</sup> According to the nanomaterials and reaction conditions, they were divided into the SNP + Laser, SNP/PEI-ICG@PEG + Laser + cooling, and SNP/PEI-ICG@PEG + Laser groups, and then the TTC color change and absorbance at 600 nm were observed for each group (Figures S4 and S5). The results showed that the MIC and MBC values of the nanomaterials were the same for *S. aureus* and *E. coli* under the same treatment conditions, revealing that the antimicrobial properties were almost indistinguishable and broad-spectrum.<sup>43</sup> The MIC and MBC values of SNP measured under laser irradiation were 4 mg/mL and 16 mg/mL, respectively. Under laser irradiation, high doses of bare SNP needed to be applied to generate enough NO and act as a sterilizing agent. However, the use of excessive concentrations of NO in antimicrobial treatment can damage normal cells.<sup>44,45</sup> Therefore, bare SNP alone was deemed unsuitable for antimicrobial treatment. The MIC and MBC values of the “SNP/PEI-ICG@PEG + laser + cooling” group were 225 µg/mL and 450 µg/mL, respectively, and those of the “SNP/PEI-ICG@PEG + laser” group were 112.5 µg/mL and 450 µg/mL, respectively. Thus, the MIC values of SNP/PEI-ICG@PEG under NIR stimulation and at different temperatures exhibited slight differences, whereas the MBC results were consistent. Based on these results, we made a bold guess—that there was a significant increase in the synergistic bactericidal effect of the multiple modes due to the increased concentration of SNP/PEI-ICG@PEG solution. It is well known that the lower the MIC and MBC values, the better the antimicrobial effect. SNP/PEI-ICG@PEG is capable of simultaneously generating mild photoheat, ROS, cations, and NO gases as a consequence of laser irradiation, with the four showing marvelous synergistic effect in antimicrobial therapy, playing the effect of “1+1+1+1>4”. SNP/PEI-ICG@PEG exhibited significant antibacterial activity and could be used as an efficient PTT/PDT/NO synergistic antibacterial therapy in vitro.

We then performed the standard plate counting assays to visualize the antimicrobial properties of the nanomaterials. We set up the following eight groups: (1) PBS, (2) SNP, (3) SNP/PEI-ICG@PEG + cooling, (4) SNP/PEI-ICG@PEG, (5)

PBS + Laser, (6) SNP + Laser, (7) SNP/PEI-ICG@PEG + Laser + cooling, (8) SNP/PEI-ICG@PEG + Laser. The nanomaterial solution in each of these groups was at a concentration of 450  $\mu\text{g/mL}$  (Figure 3). There was no statistically significant difference in the bacterial plate counts of the SNP group and the NIR-treated PBS and SNP groups when compared to the PBS group and control group, suggesting the negligible ability to kill bacteria using light alone or SNP with or without light treatment. In the “SNP/PEI-ICG@PEG + cooling” and SNP/PEI-ICG@PEG groups, the survival of *S. aureus* decreased by about 15.53% and 23.16%, respectively, and the survival of *E. coli* decreased by about 23.48% and 34.84%, respectively, owing to the positive charge on the surfaces of the nanoparticles. The “SNP/PEI-ICG@PEG + Laser + cooling” group generated ROS and NO, which reacted to form reactive nitrogen species (RNS).<sup>46</sup> This expansion of antibacterial properties was achieved by exacerbating lipid peroxidation and destroying bacterial membranes, resulting in a decrease in the survival rate of *S. aureus* by approximately 98.5% and *E. coli* by 100%. Additionally, the inhibition rate of this group was significantly higher than that of the “SNP + laser” group. When mild photothermal treatment was performed with the “SNP/PEI-ICG@PEG + Laser” group, the survival rates of *S. aureus* and *E. coli* decreased by about 99.82% and 100%, respectively; this outcome was sufficient for proving the superiority of synergistic treatment involving the four antimicrobial modalities. The plate counting results showed that the antimicrobial capacity of the nanoparticles was concentration dependent when *S. aureus* and *E. coli* were treated with different concentrations of SNP/PEI-ICG@PEG solution under NIR light. However, the difference between the survival rates of *S. aureus* and *E. coli* was not significant when subjected to the same SNP/PEI-ICG@PEG concentration, although the survival rate of *S. aureus* was greater than that of *E. coli*; this might have been due to the disruption of cell membranes by positively charged nanorods, reducing the advantage of G+ bacteria over G- bacteria due to an extra layer of cell membrane (Figures S6A and B).<sup>47,48</sup>

Live and dead bacteria can be separately stained with 9-octadecen-1-amine,N,N-dimethyl-,(9Z) (DMAO; color: green) and ethidium homodimer III (EthD-III; color: red), respectively, and their status can be clearly observed under

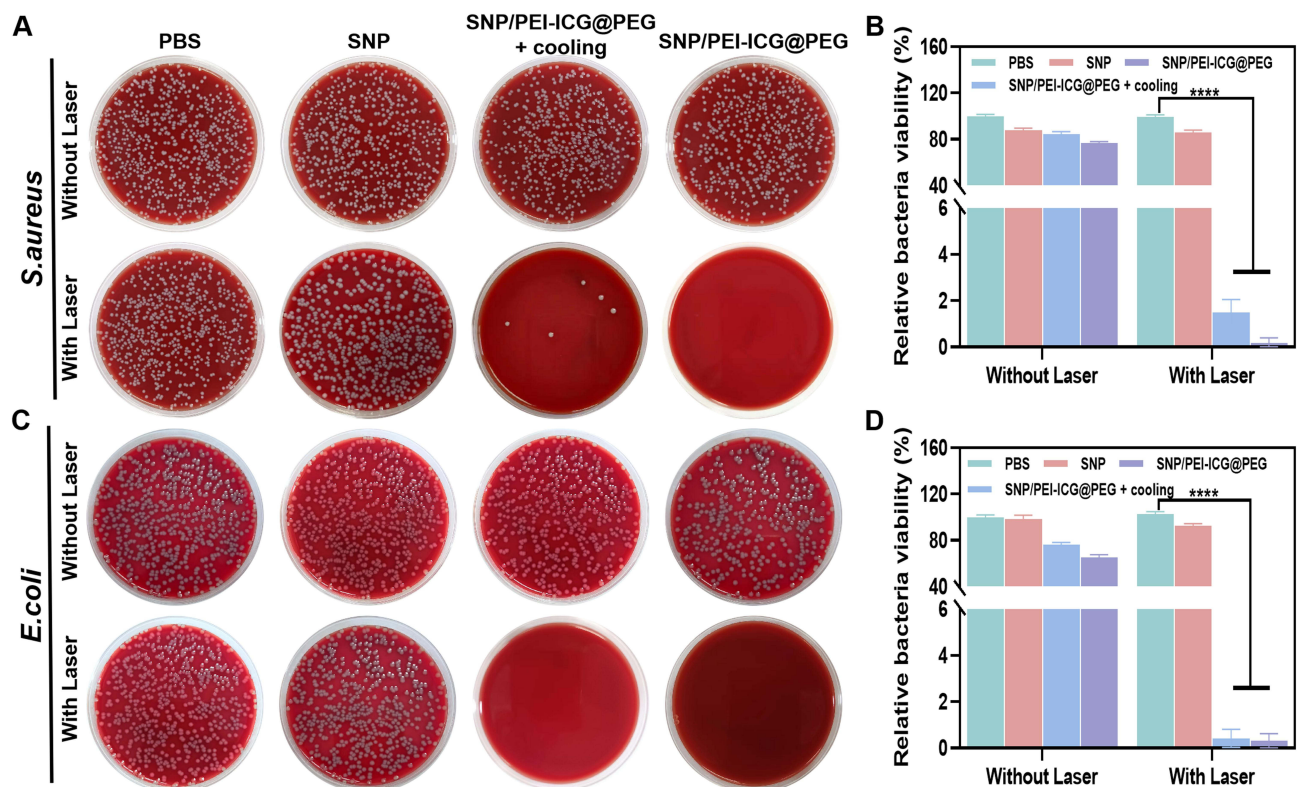


**Figure 3 (A and B)** *S. aureus* plate plots and bacterial survival percentages for the different treatment groups (PBS, SNP, SNP/PEI-ICG@PEG + cooling, SNP/PEI-ICG@PEG, PBS + laser, SNP + laser, SNP/PEI-ICG@PEG + laser + cooling, SNP/PEI-ICG@PEG + laser; The concentration of each drug was 450  $\mu\text{g/mL}$ ). **(C and D)** *E. coli* plate plots and bacterial survival percentages for the different treatment groups (PBS, SNP, SNP/PEI-ICG@PEG + cooling, SNP/PEI-ICG@PEG, PBS + laser, SNP + laser, SNP/PEI-ICG@PEG + laser + cooling, SNP/PEI-ICG@PEG + laser; The concentration of each drug was 450  $\mu\text{g/mL}$ ). Error bars represent the standard deviations determined from three independent measurements (mean  $\pm$  SD,  $n=3$ , \*\*\*\* $p < 0.0001$ ).

an inverted fluorescence microscope. We conducted a live/dead bacterial staining experiment and grouped them according to the aforementioned method. Since our ultimate goal was to kill bacteria and eliminate biofilms, the antibacterial concentration of the nanomaterials was set to 450  $\mu\text{g/mL}$ . As shown in Figure 4A and B, *S. aureus* and *E. coli* bacteria treated with PBS and naked SNP with or without light appeared green, indicating that they were alive, while the red-stained dead bacteria were almost invisible. The red color increased in fluorescence intensity in the SNP/PEI-ICG@PEG + cooling and SNP/PEI-ICG@PEG, indicating that the cationic nanorods damaged the surface structures of the bacteria, resulting in bacterial death. The “SNP/PEI-ICG@PEG + cooling” and SNP/PEI-ICG@PEG groups demonstrated an increase in fluorescence intensity of red color, illustrating that the cationic nanorods caused damage to the surface structure of the bacteria, resulting in bacterial death. The “SNP/PEI-ICG@PEG + Laser” and “SNP/PEI-ICG@PEG + cooling + Laser” groups were both red under the microscope, indicating that all the bacteria in these groups were dead, which was consistent with the MBC results.

The damage to the cell membranes of *S. aureus* and *E. coli* was observed via TEM (Figure 4C and D). The surface morphologies of *S. aureus* and *E. coli* in the PBS and PBS + Laser groups were intact, implying that the use of a single laser had no destructive effect on the bacteria. However, consistent with the results of the in vitro antibacterial experiments, the bacteria in the other treatment groups showed varying degrees of cell membrane damage. Compared

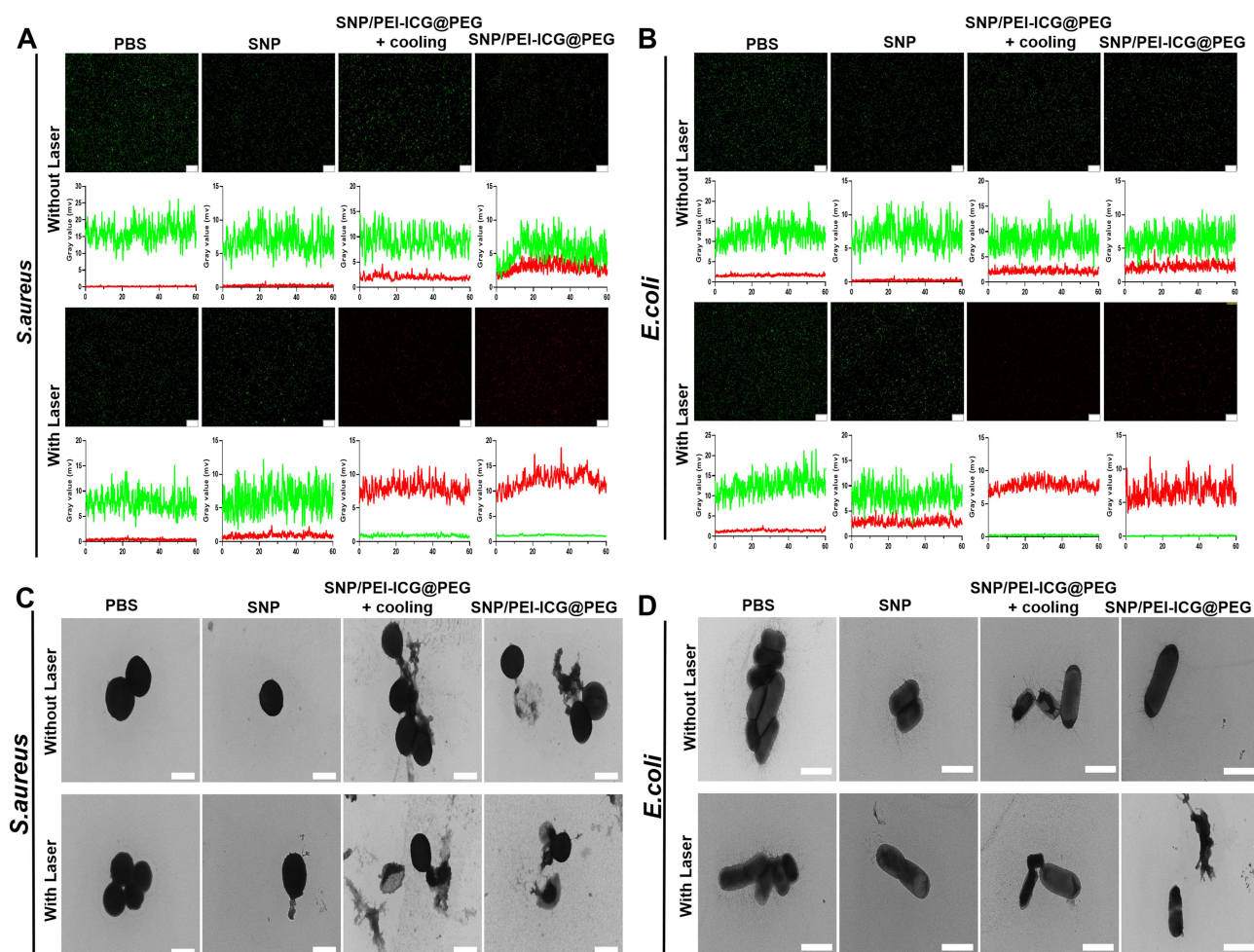


**Figure 4** (A and B) The different groups' (PBS, SNP, SNP/PEI-ICG@PEG + cooling, SNP/PEI-ICG@PEG, PBS + Laser, SNP + Laser, SNP/PEI-ICG@PEG + Laser + cooling, SNP/PEI-ICG@PEG + Laser) inverted fluorescence images of live/dead *S. aureus* and *E. coli* after treatment and fluorescence intensity quantization (The concentration of each drug was 450  $\mu\text{g/mL}$ ; scale bar=50  $\mu\text{m}$ ); (C) TEM images of *S. aureus* in the different treatment groups (PBS, SNP, SNP/PEI-ICG@PEG + cooling, SNP/PEI-ICG@PEG, PBS + Laser, SNP + Laser, SNP/PEI-ICG@PEG + Laser + cooling, SNP/PEI-ICG@PEG + Laser); The concentration of each drug was 450  $\mu\text{g/mL}$ ; scale bar=1  $\mu\text{m}$ ); (D) TEM images of *E. coli* in the different treatment groups (PBS, SNP, SNP/PEI-ICG@PEG + cooling, SNP/PEI-ICG@PEG, PBS + Laser, SNP + Laser, SNP/PEI-ICG@PEG + Laser + cooling, SNP/PEI-ICG@PEG + Laser); The concentration of each drug was 450  $\mu\text{g/mL}$ ; scale bar=2  $\mu\text{m}$ ).

to the nonlaser groups (SNP, SNP/PEI-ICG@PEG + cooling, SNP/PEI-ICG@PEG), severe morphological changes were seen in the laser-irradiated groups, with different degrees of cytoplasmic leakage. Among them, the bacterial damage in the SNP/PEI-ICG@PEG + laser group was the most significant, with a complete collapse of the cell membrane and obvious structural division. All the results further indicate that PTT/PDT/NO combined therapy has a significant effect on bacterial therapy.

## Elimination of the Formed Biofilms

The nanomaterials we designed could kill free bacteria; could they also eliminate the biofilms that had formed? To answer this question, we prepared biofilms in vitro and treated them groupwise (using the same grouping categories as above (Figure 5A)). In the absence of NIR light, the disruption of mature biofilms was negligible. It has been reported that the diffusion distance of simple ROS is only less than 0.02  $\mu\text{m}$ , which is not enough to penetrate biofilms.<sup>49</sup> However, NO can alter the structure of a biofilm and disrupt its protective barrier by decreasing the level of c-di-GMP, making ROS penetration easier. This enhances the association between multimodal antimicrobial mechanisms and accelerates the degradation of mature biofilms.<sup>50–52</sup> Thus, when NIR is present, the disruption of biofilm integrity becomes increasingly evident with the progressive combined application of cations, NO, PDT, and PTT. In the present study, biofilms formed by *S. aureus* and *E. coli* were lysed with ethanol, and the absorbance of the mixture was measured at OD 570 (Figure 5B and C). The results corresponded to the percentages of biofilm that remained, as shown in the pictures. The OD 570 values of the SNP/PEI-ICG@PEG + laser group (SNP/PEI-ICG@PEG dispersion concentration of 450  $\mu\text{g/mL}$ ) corresponded to decreases in the residual *S. aureus* and *E. coli* biofilms to 23.86% and 17.35%, respectively, relative to the PBS group. The elimination of biofilms using SNP/PEI-ICG@PEG was dose dependent (Figure S7). Excitingly, SNP/PEI-ICG@PEG was effective in killing free-living bacteria and eliminating biofilms even at low concentrations. Thus, similar doses of this drug can be used to achieve superior anti-infective therapeutic efficacy.

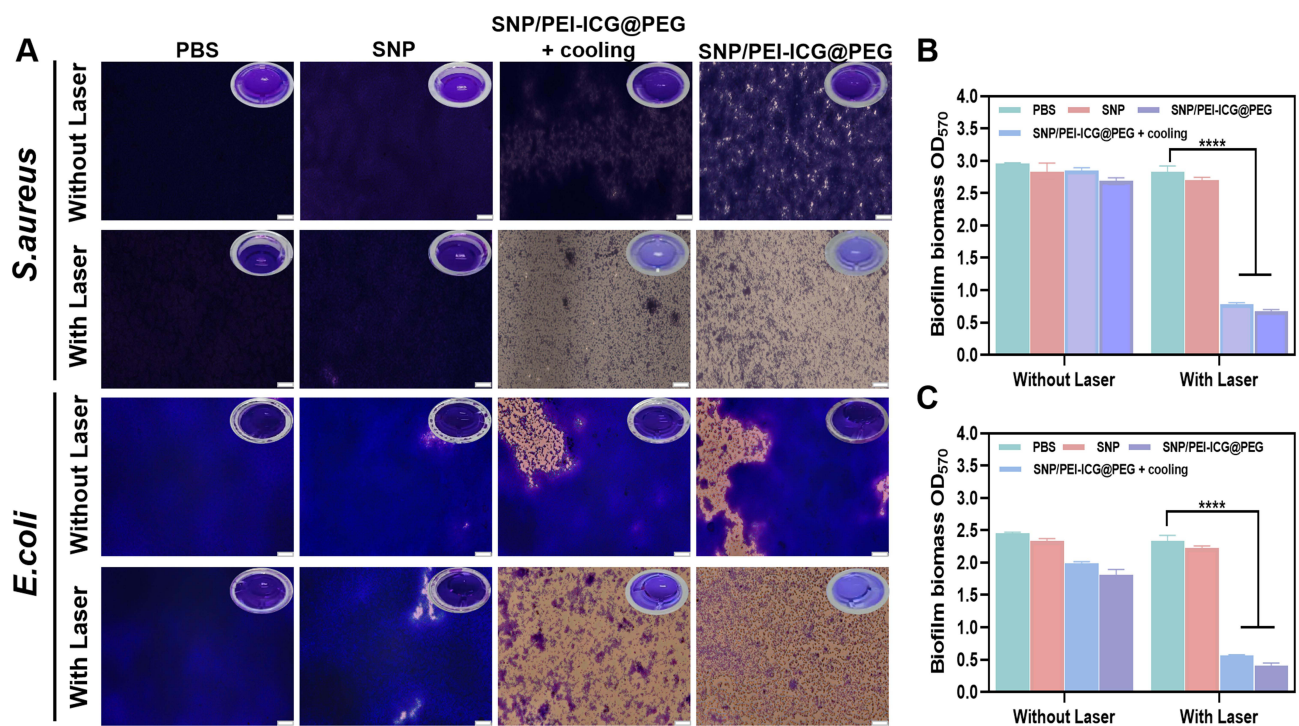


**Figure 5** (A) Biofilm inversion fluorescence imaging and biofilm imaging of the different groups after treatment (PBS, SNP, SNP/PEI-ICG@PEG + cooling, SNP/PEI-ICG@PEG, PBS + Laser, SNP+Laser, SNP/PEI-ICG@PEG + Laser + cooling, SNP/PEI-ICG@PEG + Laser; The concentration of each drug was 450  $\mu\text{g/mL}$ ; bar=50  $\mu\text{m}$ ). (B) The biofilm OD<sub>570</sub> values of *S. aureus* dissolved by ethanol. (C) The biofilm OD<sub>570</sub> values of *E. coli* dissolved by ethanol. The error bars represent the standard deviations obtained from three independent measurements (mean  $\pm$  SD, n=3; \*\*\*\*p < 0.0001).

## Biosafety Evaluation

The potential toxicity of nanomaterials is a major concern affecting their biomedical application. We assessed the cytotoxicity of the nanomaterials in the present study through hemolysis experiments and cell viability assays.<sup>53</sup> In the first hemolysis experiment (Figure 6A), the experimental group's hemolysis rate was no more than 3% compared to the positive control group, even when the concentration of SNP/PEI-ICG@PEG solution was as high as 1 mg/mL. This finding demonstrated the good blood compatibility of the nanomaterials. Subsequent experiments involved different concentrations of SNP/PEI-ICG@PEG and SNP solutions incubated with L929 cells (Figure 6B). At a concentration of 1 mg/mL, the cell viability of the L929 cells decreased to 39.12% when treated with SNP alone. However, when treated with SNP/PEI-ICG@PEG, the viability of the L929 cells remained above 80% both with and without NIR irradiation, exhibiting negligible cytotoxicity and phototoxicity (Figure 6C).

## Evaluation of Antimicrobial Properties in vivo

The success of the above experiments proved that the nanoparticles had good biosafety levels and the ability to eliminate bacteria and biofilms in vitro. Therefore, we further studied the performance of the nanoparticles in vivo.

## Evaluation of Photothermal Properties in vivo

SNP/PEI-ICG@PEG solution (450  $\mu\text{g/mL}$ , 200  $\mu\text{L}$ ) was applied onto the wounds of mice and irradiated with an 808 nm laser (1.0  $\text{W/cm}^2$ , 5 min). The temperature rise was observed in real time using an infrared thermoimager system (Figure 7A and B). After laser irradiation, the temperature of SNP/PEI-ICG@PEG on the back of the skin increased from 35.9  $^{\circ}\text{C}$  to 45  $^{\circ}\text{C}$  ( $\Delta T=9.1$   $^{\circ}\text{C}$ ), whereas the temperature of the wound treated with PBS only increased by 3.1  $^{\circ}\text{C}$ . This proved that the nanoparticles had good photothermal properties in vivo.

## In vivo Antibacterial Test

Wound model mice infected with *S. aureus* were randomly divided into five groups: (1) PBS + Laser, (2) SNP/PEI-ICG@PEG, (3) SNP + Laser, (4) SNP/PEI-ICG@PEG + Laser + cooling, and (5) SNP/PEI-ICG@PEG + Laser. The rats were treated once every two days for a total of two times, and photos of the wounds were taken on the 1st, 3rd, and 7th days to observe any changes in the wound area. Data analysis of the epithelial regeneration rates was performed using Image J software (Figure 7C and D). There was little change in the wound area between the first and third days. The wound areas of the rats in the later treatment group gradually reduced, possibly due to inflammatory infection.<sup>54</sup> On day 7, the wound area ratios of the “SNP/PEI-ICG@PEG + Laser + cooling” and “SNP/PEI-ICG@PEG + Laser” groups decreased to 17.50% and 10.37%, respectively. The wound area ratio was much higher than that of SNP/PEI-ICG@PEG and SNP + Laser (38.0% and 39.89%), further confirming the ability of SNP/PEI-ICG@PEG to initiate four synergistic antibacterial therapy modes under laser irradiation at the same time. During the treatment period, the mice were

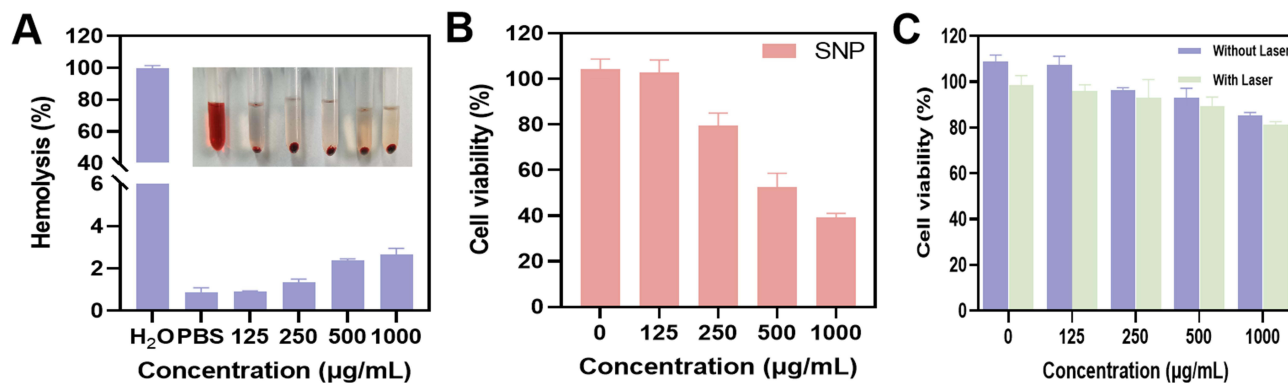


**Figure 6** (A) Hemolysis rate and pictures of SNP/PEI-ICG@PEG (concentration of drug: 0, 125, 250, 500, and 1000  $\mu\text{g/mL}$ ). (B) Survival rate of L929 cells treated with different concentrations of SNP solution (0, 125, 250, 500, and 1000  $\mu\text{g/mL}$ ). (C) Cell viability of L929 cells with different concentrations of SNP/PEI-ICG@PEG solutions (0, 125, 250, 500, and 1000  $\mu\text{g/mL}$ ) in the presence and absence of light. The error bars represent the standard deviations obtained from three independent measurements.

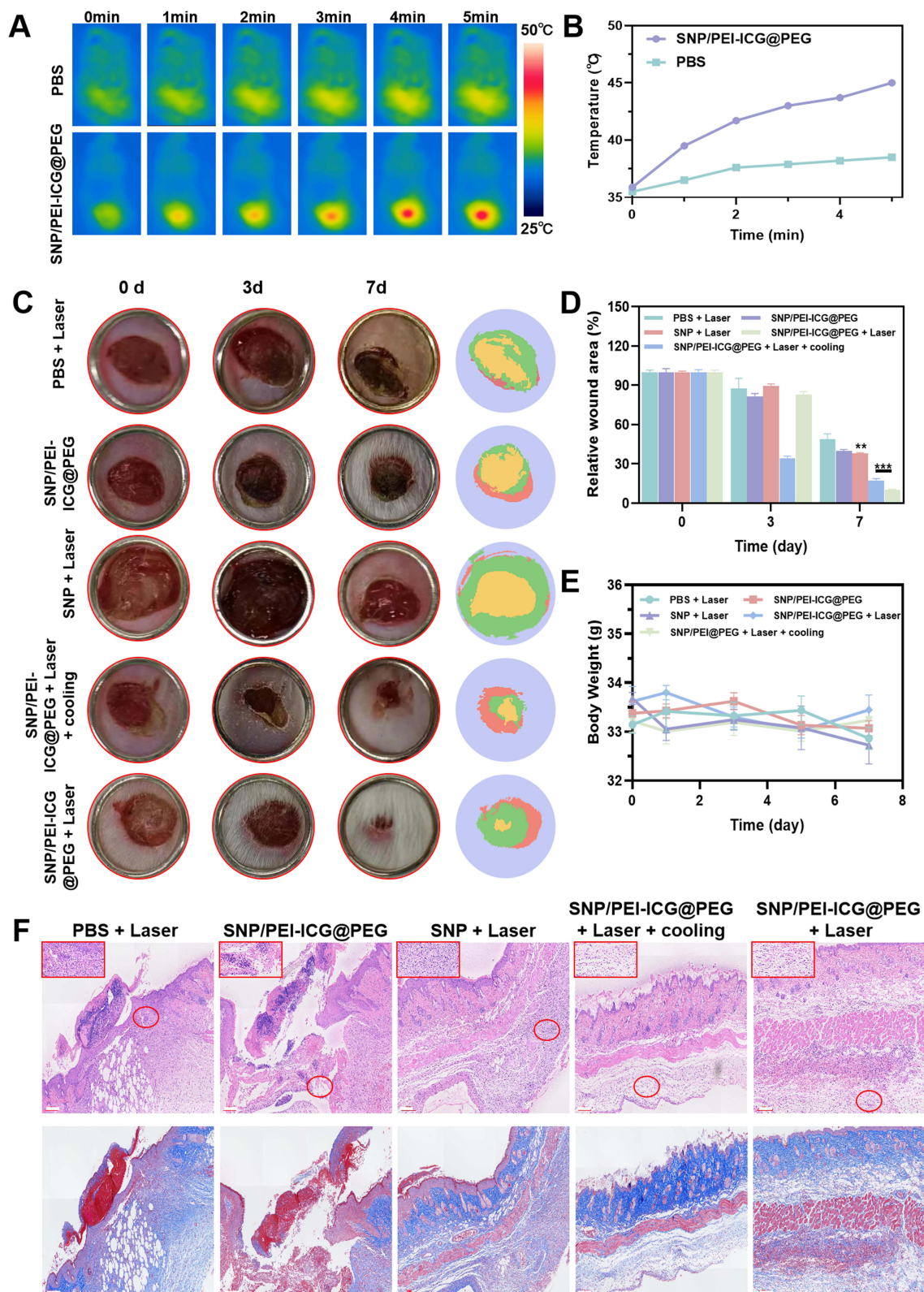


**Figure 7** (A) Thermal imaging of mice after laser irradiation. (B) Corresponding temperature curve. (C) Treatment period (0, 3, 7 days), Camera images and ImageJ rendering of Staphylococcus aureus infected wounds in different treatment groups (PBS + Laser, SNP/PEI-ICG@PEG, SNP + Laser, SNP/PEI-ICG@PEG + Laser + cooling, SNP/PEI-ICG@PEG + Laser) Wound healing diagram. (D) The statistical map of wound healing rates. (mean ± SD, n=4; \*\*P < 0.01, \*\*\*P < 0.001) (E) Weight changes during treatment (days 0, 1, 3, 5, 7; mean ± SD, n=4). (F) H&E and Masson staining of the wound tissues. (bar=100 μm).

periodically weighed, and no significant changes were observed (Figure 7E). Routine blood examinations (Figure S8) showed that the indexes for red blood cells, white blood cells, and average red blood cell volume were within the normal fluctuation ranges, similar to those of the healthy mice (control group), indicating the safety of the nanosphere materials in vivo.

On the 7th day of the experiment, the mice were killed, and the skin tissues were stained with H&E and Masson to observe the pathological changes (Figure 7F). The results showed obvious neutrophils and wound scabs in the PBS + laser, SNP/PEI-ICG@PEG, and SNP + laser groups. However, the “SNP/PEI-ICG@PEG + laser + cooling” and “SNP/PEI-ICG@PEG + laser” groups did not exhibit any obvious inflammatory cells, new blood vessel and hair follicle generation, or scar tissue.<sup>55</sup> This was likely because SNP/PEI-ICG@PEG triggered an immune response in vivo in addition to antiinfection treatment, thus releasing NO gas, promoting cell proliferation and neovascularization, enhancing collagen synthesis and deposition, and accelerating wound healing. Further, the H&E staining results of important mouse organs (heart, liver, spleen, lung, and kidney) showed no obvious histological injuries (Figure S9), demonstrating the high biosafety of SNP/PEI-ICG@PEG.

## Conclusion

We designed a nanoplatform made of cationic polymer SNP/PEI-ICG@PEG that could be triggered with an 808 nm laser to simultaneously initiate a four-in-one PTT/PDT/GT/cation treatment to eliminate free bacteria and biofilms. The therapeutic effects of this system were systematically verified through in vivo and ex vivo experiments, and the specific therapeutic principle was as follows: mild light and heat, ROS, cation, and NO gas eliminated the bacteria and biofilms through a series of molecular reactions, such as bacterial protein denaturation, DNA damage, and bacterial wall destruction. At the same time, NO destroyed the biofilms, allowing ROS to enter its interior and react to form lethal RNS molecules. We enhanced the safety of the nanoparticles by controlling excessive warming and the intermittent release of NO to avoid damage to normal cells. The excellent antimicrobial properties of this platform hold great potential for future applications in antimicrobial infection therapy.

## Ethics Approval

The animal experiments were performed in accordance with the rules of the Animal Experiment Ethics Committee of Weifang Medical University (ethics approval number: 2023SDL334). All animal studies complied with the principles based on the International Guiding Principles for Biomedical Research Involving Animals for future applications in antimicrobial infection therapy.

## Acknowledgment

This work was supported by Natural Science Foundation of Shandong (ZR2023MH293), State Administration of Traditional Chinese Medicine Science and technology department co-construction of science and technology (GZY-KJS-SD-2023-019), the “XINRUI” Project of Cancer Supportive Care and Treatment Research (cphcf-2023-076).

## Disclosure

The authors report no conflicts of interest in this work.

## References

1. Sender R, Fuchs S, Milo R. Are we really vastly outnumbered? Revisiting the ratio of bacterial to host cells in humans. *Cell*. 2016;164(3):337–340. doi:10.1016/j.cell.2016.01.013
2. Zhu B, Wang X, Li L. Human gut microbiome: the second genome of human body. *Protein Cell*. 2010;1(8):718–725. doi:10.1007/s13238-010-0093-z
3. Liu Z, Deng Y, Ji M, et al. Prophages domesticated by bacteria promote the adaptability of bacterial cells. *Biocell*. 2020;44(2):157. doi:10.32604/biocell.2020.09917
4. Yan J, Bassler BL. Surviving as a community: antibiotic tolerance and persistence in bacterial biofilms. *Cell Host Microbe*. 2019;26(1):15–21. doi:10.1016/j.chom.2019.06.002
5. Sharma D, Misra L, Khan AU. Antibiotics versus biofilm: an emerging battleground in microbial communities. *Antimicrob Resist Infect Control*. 2019;876:1–10.



6. Xu Q, Hu X, Wang Y. Alternatives to conventional antibiotic therapy: potential therapeutic strategies of combating antimicrobial-resistance and biofilm-related infections. *Mol Biotechnol.* 2021;63(12):1103–1124. doi:10.1007/s12033-021-00371-2
7. Şen Karaman D, Ercan UK, Bakay E, et al. Evolving technologies and strategies for combating antibacterial resistance in the advent of the postantibiotic era. *Adv Funct Mater.* 2020;30(15):1908783. doi:10.1002/adfm.201908783
8. Peng J, Xie S, Huang K, et al. Nitric oxide-propelled nanomotors for bacterial biofilm elimination and endotoxin removal to treat infected burn wounds. *J Mat Chem B.* 2022;10(22):4189–4202. doi:10.1039/D2TB00555G
9. Bag N, Bardhan S, Roy S, et al. Nanoparticle-mediated stimulus-responsive antibacterial therapy. *Biomater Sci.* 2023;11(6):1994–2019. doi:10.1039/D2BM01941H
10. Colino CI, Lanao JM, Gutierrez-Millan C. Recent advances in functionalized nanomaterials for the diagnosis and treatment of bacterial infections. *Mater Sci Eng C.* 2021;121:111843.
11. Jia B, Du X, Wang W, et al. Nanophysical antimicrobial strategies: a rational deployment of nanomaterials and physical stimulations in combating bacterial infections. *Adv Sci.* 2022;9(10):e2105252. doi:10.1002/advs.202105252
12. Kwiatkowski S, Knap B, Przystupski D, et al. Photodynamic therapy - mechanisms, photosensitizers and combinations. *Biomed. Pharmacother.* 2018;106:1098–1107.
13. Makabenta JMV, Nabawy A, H LC, et al. Nanomaterial-based therapeutics for antibiotic-resistant bacterial infections. *Nat Rev Microbiol.* 2021;19(1):23–36. doi:10.1038/s41579-020-0420-1
14. Bilici K, Atac N, Muti A, et al. Broad spectrum antibacterial photodynamic and photothermal therapy achieved with indocyanine green loaded SPIONs under near infrared irradiation. *Biomater Sci.* 2020;8(16):4616–4625. doi:10.1039/D0BM00821D
15. Li Y, Liu X, Cui Z, et al. Treating multi-drug-resistant bacterial infections by functionalized nano-bismuth sulfide through the synergy of immunotherapy and bacteria-sensitive phototherapy. *ACS nano.* 2022;16(9):14860–14873. doi:10.1021/acsnano.2c05756
16. Zhou B, Sun X, Dong B, et al. Antibacterial PDT nanoplatfrom capable of releasing therapeutic gas for synergistic and enhanced treatment against deep infections. *Theranostics.* 2022;12(6):2580–2597. doi:10.7150/thno.70277
17. Sun B, Ye Z, Zhang M, et al. Light-activated biodegradable covalent organic framework-integrated heterojunction for photodynamic, photothermal, and gaseous therapy of chronic wound infection. *ACS Appl Mater Interfaces.* 2021;13(36):42396–42410. doi:10.1021/acsmi.1c10031
18. Huang S, Liu H, Liao K, et al. Functionalized GO nanovehicles with nitric oxide release and photothermal activity-based hydrogels for bacteria-infected wound healing. *ACS Appl Mater Interfaces.* 2020;12(26):28952–28964.
19. Wang K, Jiang L, Qiu L. Near infrared light triggered ternary synergistic cancer therapy via L-arginine-loaded nanovesicles with modification of PEGylated indocyanine green. *Acta Biomater.* 2022;140:506–517.
20. Xin Y, Yu Y, Su M, et al. In situ-activated photothermal nanoplatfrom for on-demand NO gas delivery and enhanced colorectal cancer treatment. *J Control Release.* 2023;35:969–984.
21. Hossain S, Nisbett LM, Boon EM. Discovery of two bacterial nitric oxide-responsive proteins and their roles in bacterial biofilm regulation. *Acc Chem Res.* 2017;50(7):1633–1639. doi:10.1021/acs.accounts.7b00095
22. Liang Z, Liu W, Wang Z, et al. Near-infrared laser-controlled nitric oxide-releasing gold nanostar/hollow polydopamine Janus nanoparticles for synergistic elimination of methicillin-resistant Staphylococcus aureus and wound healing. *Acta Biomater.* 2022;143:428–444.
23. Wu X, Qi M, Liu C, et al. Near-infrared light-triggered nitric oxide nanocomposites for photodynamic/photothermal complementary therapy against periodontal biofilm in an animal model. *Theranostics.* 2023;13(7):2350–2367. doi:10.7150/thno.83745
24. Seabra AB, Justo GZ, Haddad PS. State of the art, challenges and perspectives in the design of nitric oxide-releasing polymeric nanomaterials for biomedical applications. *Biotechnol Adv.* 2015;33(6 Pt 3):1370–1379. doi:10.1016/j.biotechadv.2015.01.005
25. Cao W, Yue L, Khan IM, Wang Z. Polyethylenimine modified MoS<sub>2</sub> nanocomposite with high stability and enhanced photothermal antibacterial activity. *J Photochem Photobiol A.* 2020;401:112762. doi:10.1016/j.jphotochem.2020.112762
26. Giano MC, Ibrahim Z, Medina SH, et al. Injectable bioadhesive hydrogels with innate antibacterial properties. *Nat Commun.* 2014;5:40:95.
27. Guan X, Guo Z, Wang T, et al. A pH-responsive detachable PEG shielding strategy for gene delivery system in cancer therapy. *Biomacromolecules.* 2017;18(4):1342–1349. doi:10.1021/acs.biomac.7b00080
28. Lv R, Yang P, He F, et al. An imaging-guided platform for synergistic photodynamic/photothermal/chemo-therapy with pH/temperature-responsive drug release. *Biomaterials.* 2015;63:115–127.
29. Huang W, Hu B, Yuan Y, et al. Visible light-responsive selenium nanoparticles combined with sonodynamic therapy to promote wound healing. *ACS Biomater Sci Eng.* 2023;9(3):1341–1351. doi:10.1021/acsbomaterials.2c01119
30. Schulze J, Kuhn S, Hendriks S, Schulz-Siegmund M, Polte T, Aigner A. Spray-Dried Nanoparticle-in-Microparticle Delivery Systems (NiMDS) for Gene Delivery, Comprising Polyethylenimine (PEI)-Based Nanoparticles in a Poly(Vinyl Alcohol) Matrix. *Small.* 2018;14(12):e1701810. doi:10.1002/sml.201701810
31. Richard I, Thibault M, De Crescenzo G, Buschmann MD, Lavertu M. Ionization behavior of chitosan and chitosan-DNA polyplexes indicate that chitosan has a similar capability to induce a proton-sponge effect as PEI. *Biomacromolecules.* 2013;14(6):1732–1740. doi:10.1021/bm4000713
32. Mohammadinejad R, Dadashzadeh A, Moghassemi S, et al. Shedding light on gene therapy: carbon dots for the minimally invasive image-guided delivery of plasmids and noncoding RNAs - A review. *J Adv Res.* 2019;18:81–93. doi:10.1016/j.jare.2019.01.004
33. Schulze J, Hendriks S, Schulz-Siegmund M, Aigner A. Microparticulate poly(vinyl alcohol) hydrogel formulations for embedding and controlled release of polyethylenimine (PEI)-based nanoparticles. *Acta Biomater.* 2016;45:210–222. doi:10.1016/j.actbio.2016.08.056
34. Cai M, Wang Y, Wang R, et al. Antibacterial and antibiofilm activities of chitosan nanoparticles loaded with Ocimum basilicum L. essential oil. *Int J Biol Macromol.* 2022;202:122–129. doi:10.1016/j.ijbiomac.2022.01.066
35. Li G, Yuan S, Deng D, et al. Fluorinated polyethylenimine to enable transmucosal delivery of photosensitizer-conjugated catalase for photodynamic therapy of orthotopic bladder tumors postintravesical instillation. *Adv Funct Mater.* 2019;29(40):1901932. doi:10.1002/adfm.201901932
36. Zhang X, He Z. Cell membrane coated pH-responsive intelligent bionic delivery nanoplatfrom for active targeting in photothermal therapy. *Int j Nanomed.* 2023;18:7729–7744. doi:10.2147/IJN.S436940
37. Feng T, Wan J, Li P, et al. A novel NIR-controlled NO release of sodium nitroprusside-doped Prussian blue nanoparticle for synergistic tumor treatment. *Biomaterials.* 2019;214:119213.
38. Theune LE, Buchmann J, Wedepohl S, et al. NIR- and thermo-responsive semi-interpenetrated polypyrrole nanogels for imaging guided combinational photothermal and chemotherapy. *J Control Release.* 2019;311–312:147–161. doi:10.1016/j.jconrel.2018.12.014

39. Cao J, Hlaing SP, Lee J, et al. Bacteria-adhesive nitric oxide-releasing graphene oxide nanoparticles for MRPA-infected wound healing therapy. *ACS Appl Mater Interfaces*. 2022;14(45):50507–50519. doi:10.1021/acsami.2c13317
40. Wang W, Ding D, Zhou K, et al. Prussian blue and collagen loaded chitosan nanofibers with NIR-controlled NO release and photothermal activities for wound healing. *J Mater Sci Technol*. 2021;93:17–27. doi:10.1016/j.jmst.2021.03.037
41. Jin F, Qi J, Liu D, et al. Cancer-cell-biomimetic Upconversion nanoparticles combining chemo-photodynamic therapy and CD73 blockade for metastatic triple-negative breast cancer. *J Control Release*. 2021;337:90–104.
42. Ma Y, Xu H, Sun B, et al. pH-responsive oxygen and hydrogen peroxide self-supplying nanosystem for photodynamic and chemodynamic therapy of wound infection. *ACS Appl Mater Interfaces*. 2021;13(50):59720–59730. doi:10.1021/acsami.1c19681
43. Singh SB, Young K, Silver LL. What is an “ideal” antibiotic? Discovery challenges and path forward. *Biochem Pharmacol*. 2017;133:63–73.
44. Bai Q, Wang M, Liu J, et al. Porous molybdenum nitride nanosphere as carrier-free and efficient nitric oxide donor for synergistic nitric oxide and chemo/sonodynamic therapy. *ACS Nano*. 2023;17(20):20098–20111. doi:10.1021/acsnano.3c05790
45. Kim S, Lee DG. PMAP-23 triggers cell death by nitric oxide-induced redox imbalance in Escherichia coli. *Biochim Biophys Acta Gen Subj*. 2019;1863(7):1187–1195. doi:10.1016/j.bbagen.2019.04.014
46. Jiang D, Pan L, Yang X, et al. Photo-controllable burst generation of peroxyxynitrite based on synergistic interactions of polymeric nitric oxide donors and IR780 for enhancing broad-spectrum antibacterial therapy. *Acta Biomater*. 2023;159:259–274. doi:10.1016/j.actbio.2023.01.032
47. Li S, Cui S, Yin D, et al. Dual antibacterial activities of a chitosan-modified upconversion photodynamic therapy system against drug-resistant bacteria in deep tissue. *Nanoscale*. 2017;9(11):3912–3924. doi:10.1039/C6NR07188K
48. Liu Y, Guo Z, Li F, et al. Multifunctional magnetic copper ferrite nanoparticles as fenton-like reaction and near-infrared photothermal agents for synergetic antibacterial therapy. *ACS Appl Mater Interfaces*. 2019;11(35):31649–31660. doi:10.1021/acsami.9b10096
49. Kipshidze N, Yeo N, Kipshidze N. Photodynamic therapy for COVID-19. *Nat Photonics*. 2020;14(11):651–652. doi:10.1038/s41566-020-00703-9
50. Lv X, Jiang J, Ren J, et al. Nitric oxide-assisted photodynamic therapy for enhanced penetration and hypoxic bacterial biofilm elimination. *Adv Healthcare Mater*. 2023;12(29):e2302031. doi:10.1002/adhm.202302031
51. Xiu W, Wan L, Yang K, et al. Potentiating hypoxic microenvironment for antibiotic activation by photodynamic therapy to combat bacterial biofilm infections. *Nat Commun*. 2022;13(1):3875. doi:10.1038/s41467-022-31479-x
52. Yang D, Ding M, Song Y, et al. Nanotherapeutics with immunoregulatory functions for the treatment of bacterial infection. *Biomater Res*. 2023;27(1):73. doi:10.1186/s40824-023-00405-7
53. Sun Q, Yang Z, Lin M, et al. Phototherapy and anti-GITR antibody-based therapy synergistically reinvigorate immunogenic cell death and reject established cancers. *Biomaterials*. 2021;269:120648.
54. Wang X, Fan G, Guan Q, et al. Hyaluronic acid-modified zif-8 nano-vehicle for self-adaption release of curcumin for the treatment of burns. *ACS Appl Nano Mater*. 2022;5(11):16094–16107. doi:10.1021/acsnm.2c02706
55. Yang K, Ding M, Xiu W, et al. Two-dimensional ternary chalcogenide nanodots with spatially controlled catalytic activity for bacteria infected wound treatment. *J Colloid Interface Sci*. 2024;657:611–618. doi:10.1016/j.jcis.2023.12.020

International Journal of Nanomedicine

Dovepress

## Publish your work in this journal

The International Journal of Nanomedicine is an international, peer-reviewed journal focusing on the application of nanotechnology in diagnostics, therapeutics, and drug delivery systems throughout the biomedical field. This journal is indexed on PubMed Central, MedLine, CAS, SciSearch®, Current Contents®/Clinical Medicine, Journal Citation Reports/Science Edition, EMBase, Scopus and the Elsevier Bibliographic databases. The manuscript management system is completely online and includes a very quick and fair peer-review system, which is all easy to use. Visit <http://www.dovepress.com/testimonials.php> to read real quotes from published authors.

Submit your manuscript here: <https://www.dovepress.com/international-journal-of-nanomedicine-journal>